Research Article Vol. 28, No. 1 / 6 January 2020 / Optics Express 116
Optics EXPRESS

Optimization of Seebeck nanoantenna-based infrared harvesters

EDGAR BRIONES,[1,*] RIEMANN RUIZ-CRUZ,[1] JOEL BRIONES,[2] AND JORGE SIMON[3]

[1]*Department of Mathematics and Physics, The Jesuit University of Guadalajara, Jalisco 45604, Mexico*
[2]*Centro de Investigaciones en Optica, Leon, Guanajuato 37150, Mexico*
[3]*Centro de Investigación, Innovación y Desarrollo en Telecomunicaciones, Universidad Autónoma de Zacatecas, Zacatecas 98000, Mexico*
[*]*edgarbriones@iteso.mx*

Abstract: In this letter, the authors develop an optimized Seebeck nanoantenna design suitable for IR harvesting applications. The design is optimized via the so-called particle-swarm-optimization algorithm (PSO), an evolutionary algorithm able to drive the morphology of a nano-object towards an optimum. Along with the so-called nanoloading technique, efforts are subsequently addressed to understand the physical mechanisms behind the wave energy to voltage conversion, from both numerical and theoretical perspectives. In particular, the thermal and intrinsic impedance are considered to be the key issues beneath the device's response.

1. Introduction

In the recent decades, important efforts have been addressed to improve the efficiency of photovoltaic devices since their worldwide demand has been growing steadily, mainly due their significant impact on the energy sector as well and their commercial applications [1]. These efforts have led, for instance, to the design and fabrication of a wide variety of semiconductor hetero-structures [2,3], which can harvest - into DC power - the optical energy of both the UV-Vis and the near-infrared bands (0.4 μm to 2.5 μm [4,5]). In this way, the crystalline silicon solar cells are the most commercialized photovoltaics devices thanks to their remarkably low-cost [6]. Nevertheless, multi-junctions cells with higher efficiencies and cost find more sophisticated applications [7].

Despite the maturity of the photovoltaic technologies, drastic limitations arise when their use as harvesters is extended to the mid-wavelength (3 μm to 8 μm) and long-wavelength (8 μm to 15 μm) infrared bands. These limitations are linked to the band gap of the semiconductor materials, which blocks the absorption of low-energy infrared photons (<0.4 eV, or wavelengths above 3 μm) [8]. Recent efforts are being conducted to develop semiconductor heterostructures whose band lies in the middle of the gap, allowing therefore such transitions [9–11]. However, these devices require sophisticated fabrication tools and their design is still under development [12,13]. Thus, in order to recover the energy of the long-wavelength (LWIR) bands, other harvesting mechanism should be explored.

On the other hand, thermocouples are quite simpler devices which recently re-appeared as promising candidates to cover the lack of a LWIR harvest technology, by gathering heat into DC power [14–16]. Thanks to the simplicity of their design, they can be taken to the nanometer scale for adopting the shape of standard LWIR resonant nano-antennas [17–19]. At that scale, thermocouples will match the infrared energy into a resonant AC mode (by the antenna-like effect) and will generate a Seebeck voltage thanks to the thermoelectric properties of their metallic interfaces [17,19,20]. In contrast to their rectennas counterpart, these devices exploit as a source the heat generated by Joule effect (due to the resonance modes), leading to efficiencies of interest for harvesting applications [15,18].

#380753 https://doi.org/10.1364/OE.380753
Journal © 2020 Received 23 Oct 2019; revised 14 Dec 2019; accepted 14 Dec 2019; published 23 Dec 2019

Optics EXPRESS

The success of the practical application of Seebeck nanoantennas relies on the implementation of the antenna architecture with high conversion efficiency. With this aim, several types of antenna designs, widely used in RF applications, have been scaled-down to infrared frequencies with the purpose of evaluating their performance as harvesters [20,21]. Despite this, the significant improvement of these devices lacks of a clear understanding of the physical mechanisms behind their performance, and calls for an efficient schema to propose interesting designs.

In this letter, the authors introduce an effective computational tool in order to obtain a Seebeck antenna design suitable for IR harvesting applications. From this, the authors conduct efforts to understand the underlying physical mechanisms, from both numerical and theoretical perspectives. In particular, the thermal and intrinsic impedances are here considered to be the key issues beneath the devices response. To this end, the authors make use of the so-called particle-swarm-optimization algorithm (PSO), an evolutionary algorithm able to drive the morphology of a nano-object towards an optimum, through several cycles that mimic social rules [22,23]. Since the geometry of the Seebeck antennas strongly affects their resonance modes (and thus their receiving properties) as well as their thermal behavior (via their steady state heat distribution), the PSO algorithm appears a suitable tool due to its ability to simultaneously target multiple-objectives.

The authors consider the use of the so-called tapered dipole geometry, a key element that allows us to advance on the purposes of this letter. The tapered dipole is a type of nano-antenna design recently introduced for harvesting applications, in which the arms forming the dipole decrease stepwise [24,25]. In contrast to other relevant antenna designs, this geometry exhibits a multi-resonance behavior; hence several current paths could be defined through its resonance modes. These properties can be tuned via the geometrical parameters, they are here thereby exploited to optimize the Joule heating and, subsequently, the DC output of the antennas.

Following this introduction, we present in section (2) a strategy to obtain the impedance of tapered bimetallic dipoles and hereupon evaluate their resonant properties in a correct manner. A description of the thermal effects that the light induces on these types of structures, as well as the evaluation of the Seebeck voltages, are resumed in section (3). Subsequently, in section (4), a particle swarm optimization algorithm (PSO) is strategically used to find the geometrical parameter that optimizes the Seebeck response of the antenna. Finally, in section (5) and section (6), we present an analysis for determining which parameters affect the most the Seebeck voltage, with stress aimed at unveiling the physical mechanism behind it.

2. Intrinsic and input impedances of emitting bimetallic dipoles

In order to address the above issues, the authors introduce a LWIR tapered dipole composed of two short-circuited arms of dissimilar metals, as shown in Fig. 1. The tapered design consists of a conventional half-wave dipole with two additional steps of smaller size inserted in each arm. Therefore, its geometrical description requires the use of a seven-dimensional space, defined by the length (L_1, L_2, L_3), the width (W_1, W_2, W_3) and the thickness T of the tapered sections.

To begin our study we have chosen a set of dimensions ($L_1 = 600$ nm, $L_2 = 300$ nm, $L_3 = 100$ nm, $W_1 = 200$ nm, $W_2 = 150$ nm, $W_3 = 100$ nm, and $T = 100$ nm), properly adjusted to recover the wavelengths around ~10.6 μm (~28.3 THz). These dimensions define a dipole with a total length $L = 2$ μm. The left and right arms of the dipole are made of nickel and titanium respectively, defining thus a thermocouple interface at the antenna center. These metals are chosen because of the high difference in their Seebeck coefficients, as well as their low thermal conductivities [26,27]. The dipole lies on the surface of a silicon dioxide wafer (SiO_2 semi-infinite) that acts as a good thermal and electric insulator [28,29], while the upper half-space is air.

To advance on this study, we must first analyze the receiving properties of the short-circuited bimetallic dipole hereby proposed. We would like to highlight that, contrary to the several relevant contributions reported on the properties of one-single metal nanometer antennas [30–32],

Optics EXPRESS

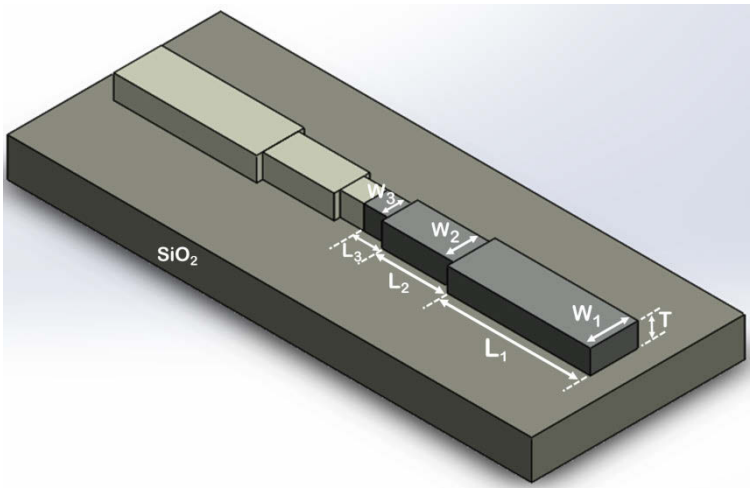

Fig. 1. Schematic representation of the three-steps tapered dipole antenna, defining its geometrical parameters width W, length L and thickness T, for each of the three steps. The LWIR tapered dipole is composed of two short-circuited arms of dissimilar metals, nickel (light gray color) and titanium (dark gray color), laying on the surface of a silicon dioxide wafer (SiO_2 semi-infinite), that acts as a good thermal and electric insulator, while the upper half-space is air.

few efforts have been addressed to the systematic study of the antennas composed by arms of dissimilar metals.

Similar to the RF antennas, the emitting and receiving properties of the nano-antennas are entirely determined by their intrinsic impedance $Z_{dip} = R_{dip}$ - j*X_{dip} [33–35]. The nature of their resonance modes and frequencies could be easily determined from their characteristic curve $Z_{dip} = Z_{dip}$ (f_E); with f_E being the frequency of the incident electromagnetic wave (for a receiving antenna) or the frequency of the port (for a transmitting antenna). Therefore, in order to tailor the resonance modes of the tapered dipole here proposed, we must conduct efforts to find this fundamental parameter for the first time.

To perform this task, we leverage the concept of *lumped nanometer-loads* feeding a nanometer antenna, recently developed by Alu *et al*. [34], as a means to tune the scattering properties of nanoantennas in the visible regime [34,36]. This *nanoloading* technique is extremely suitable for the impedance analysis of nanodipoles made of dissimilar metals. Their extended use to the case of Seebeck antennas in the LWIR regime is here thereby considered.

The *nanoloading* technique is here considered by introducing the open-circuit dipole shown in Fig. 2(a), featuring an air-gap at its center ($G = 50$nm), which acts as a *nanoload* element. The dimensions and materials of the open-circuit dipole are the same than those of the short-circuit dipole in Fig. 1, with the exception of the inner step length (L_3), which results reduced by the gap. As sketched in the inset of Fig. 2(a), the input impedance $Z_{in} = R_{in}$ - j*X_{in} of the open-circuit dipole may be interpreted as the parallel combination of the dipole intrinsic impedance Z_{dip} and the air-gap impedance Z_{GAP} introduced by the gap [33]. In this way, the intrinsic impedance Z_{dip} of the short-circuit dipole can be evaluated if the input impedance Z_{in} and the gap impedance Z_{GAP} are known. Below, we introduce the strategies used to obtain both parameters.

The input impedance Z_{in} of the air-gap dipole in Fig. 2(a) can be obtained by driving the terminals of the antenna with an alternate voltage V_{AC} and subsequently obtaining the current I_{AC} that flows through the dipole terminals. By this means, the impedance is easily evaluated by the ratio $Z_{in} = V_{AC}/I_{AC}$. This procedure cannot be performed by means of receiving simulations

Optics EXPRESS

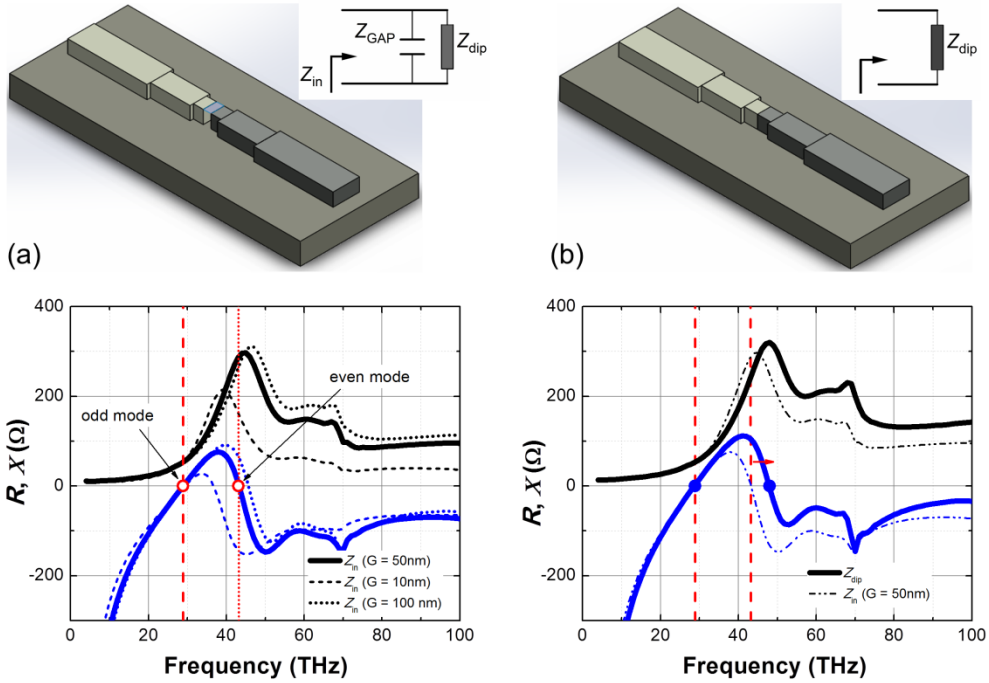

Fig. 2. Schematic representation (*top*) and frequency dependence of the characteristic impedance (*bottom*) of: (a) the open-circuit dipole bimetallic nano-antenna, loaded with an air-gap of size G; and (b) the short-circuited dipole bimetallic nano-antenna. R and X correspond to the real and imaginary parts of the impedance, respectively. The resonant modes of the antenna are those frequencies for which the reactance R vanishes. The fundamental (*odd*) and the harmonic (*even*) modes are indicated by the circles.

in which the dipole is illuminated by external sources, therefore, we perform simulations in the transmit mode of the antenna. These simulations are performed by using the COMSOL Multi-Physics (ver5.4a) software package based on the finite-element method. Thanks to this package, we can use a lumped port element at the gap of the dipole, marked in blue in the Fig. 2(a), to drive the arms of the antenna with a sinusoidal voltage of amplitude $V_{AC} = 1$ V; the impedance of the port Z_0 is arbitrary adjusted to 50 Ω. By sensing both, the amplitude and the phase of the induced alternate current at the port, the software package performs a one-port analysis to evaluate the input impedance Z_{in}. On the other hand, because of the strong dispersion in metals at optical frequencies, the numerical model is built by using the dielectric function of materials reported in literature [37]. Moreover, since the emitting dipole radiates electromagnetic energy towards its surroundings, which could reflect (at the boundaries of the simulation space) and thus perturb the sensed current, we have defined the boundaries as perfect absorbers (PML layers). The graph at the bottom of Fig. 2(a) presents the results obtained for the input resistance R_{in} (marked in black) and the reactance X_{in}, of the dipole (marked in blue). These values correspond to the real and imaginary parts of the input impedance, respectively.

Once the input impedance Z_{in} of the dipole in Fig. 2(a) was evaluated, the current resonance modes can be easily determined from this plot. In general, the resonances of emitting dipoles are defined as the frequencies where the reactance goes to zero [38]; consequently, only the real part contributes to the antenna input impedance. In these cases (when $X_{in} = 0$), the voltage across the input port V_{AC} is in phase with the current I_{AC} induced along the dipole. The simulations in Fig. 2(a) unveil in a clear manner that the tapered dipole holds two resonances, the first one at

Optics EXPRESS

~28 THz and the second one at ~43 THz (remarked with open circles). On the one hand, the first resonance (~28 THz) is known as the *odd mode* or as the *series resonance* (commonly described by a series RCL equivalent-circuit [33,38]). For this mode, the derivative of the reactance with respect to frequency is positive, and the impedance exhibits a low value $Z_{in} \sim 50\Omega$. Consequently, the current at the port reaches its greatest effective value, and the current distribution exhibits two nodes at the ends of the dipole. On the other hand, the second resonance (~43 THz) is known as the *even mode* or as the *parallel resonance* (commonly described by a parallel RCL-circuit [33,38]). In contrast to the *odd mode*, the derivative of the reactance for the *even mode* is negative, and the impedance exhibits a high value $Z_{\text{in}} \sim 286\ \Omega$. Consequently, the current at the port reaches its minimum value, so, the current distribution exhibit three nodes, two at the ends of the dipole, and one at the center of the dipole (or port).

Furthermore, we must note that the presence of the air-gap impedance Z_{GAP}, which nature is entirely capacitive, results in the shift of both the input impedance Z_{in} and the resonance modes toward lower frequencies [33].

On the one hand, the value of the impedance Z_{GAP} can be tuned by means of the gap size G [39,40]: shorter gaps induce higher gap capacitances, hence, larger shifts toward lower frequencies of the input impedance Z_{in} and the resonance mode. This behavior is clearly seen in the numerical results shown in Fig. 2(b), where the impedance Z_{in} is plotted for two different gap sizes (10 and 100 nanometers). In this way, a gap with a shorter (longer) length exhibits an input impedance at lower (higher) frequencies. It must be noted, that only the *even* resonance mode shifts towards higher frequencies, in contrast to the *odd* mode that does not. This fact is clarified below.

On the other hand (and more important for this study), the value of the impedance Z_{GAP} can be obtained by means of numerical simulations and then be used to remove it from the Z_{in}, and subsequently obtain the intrinsic impedance Z_{dip} through the relationship:

$$Z_{dip} = (Z_{in} * Z_{GAP})/(Z_{GAP} - Z_{in}) \tag{1}$$

By doing so, both the resistance R_{dip} and reactance X_{dip}, corresponding to the dipole intrinsic impedance Z_{dip}, have been determined and plotted (in bold line) in Fig. 2(b).

The numerical results clearly show that both the input X_{in} and the intrinsic X_{dip} reactance plots hit the first zero at the same frequency ~ 28 THz ($\lambda \sim 10.6$ μm). This implies that both dipoles exhibit (almost) the same *odd mode* regardless of whether or not a gap is present [33]. The *odd mode* is the first available natural resonance of the bimetallic dipole, the so-called "short-circuit resonance," which occurs when the intrinsic reactance of the dipole X_{dip} vanishes, and thus being (almost) unaffected by any variation of the gap capacitance [34]. At the frequency ~ 48 THz, the intrinsic impedance of the bimetallic dipole Z_{dip} shows an *even* resonance mode, the so-called "open-circuit resonance," which holds an important large impedance [34,36]. The non-negligible gap impedance Z_{GAP} then resonates with the *even* mode of Z_{dip}, shifting the *even* mode of the input impedance Z_{in}, as stated above [36].

It is worth to note that the input impedance of the bimetallic dipole, shown in Fig. 2(a), which presents a gap, is employed to get the intrinsic impedance counterpart. This impedance Z_{dip} corresponds to the impedance of the continuous bimetallic dipole shown in Fig. 2(b). Such a dipole consists of two arms joined together to conform a thermocouple so-called Seebeck dipole (with a total length of $L = 2$ μm). Such a structure is able to generate a Seebeck voltage, parameter evaluated below.

3. Bimetallic receiving dipoles and thermal gradients

Once we have introduced a strategy to get the intrinsic impedance of short-circuited tapered dipoles Z_{dip}, the next step involves determining (by numerical simulations) the temperature distribution caused in the devices by the incident light, and so, to determine the Seebeck DC

Optics EXPRESS

voltage that the dipoles generate at their ends. Particularly, we conduct efforts to evaluate the dipole performance under the illumination of a single monochromatic plane wave of 10.6 μm. Prior to it, we must note that, similar to the half-wave dipoles the short-circuited tapered dipoles will respond to linearly polarized light [24,25]; this, because of their linear axes. Therefore, in order to excite the devices we make use of a monochromatic linearly polarized (LP) plane wave whose electric field (of arbitrary intensity) is parallel to the dipole axis.

On the other hand, and more important for this study, when the short-circuited dipole in Fig. 2(b) is illuminated by the LP plane wave, the optical energy can be turned into an alternate current only by exciting the *odd mode*. This means that the light only interacts with the *odd mode* and not with the *even mode* [36,38]; this, only in the case of short-circuited dipoles (since open-circuit dipoles only interact with *even modes*). To confirm this, we present the numerical results in Fig. 3(a), plotted by using a bold line. To obtain those results, we have excited the dipole with a monochromatic plane wave (of a single frequency) and have evaluated the power dissipated along the device by ohmic losses. We have repeated this procedure for different values of the plane wave frequency, leading to the results in Fig. 3(a). The figure-of-merit provides indirect information about the resonance mode of the dipole; in particular, the single frequency that maximizes the dissipation of power by ohmic losses is expected to be near the frequency of the odd resonance mode [41,42]. This occurs for a frequency ~26 THz (~10.6 μm), which certainly matches the resonance frequency value obtained by the correct method presented above.

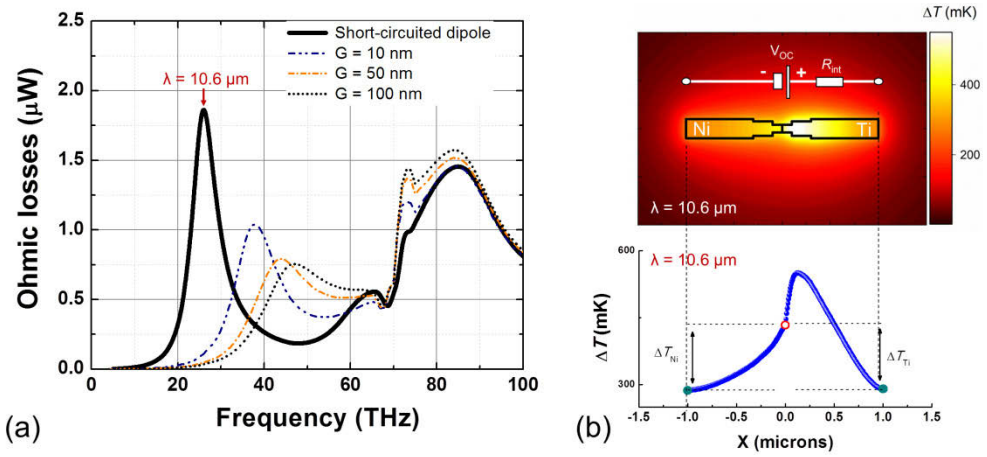

Fig. 3. Thermal response of the short-circuited tapered dipole antenna when illuminated by an external source. (a) Frequency dependence of the ohmic losses. For comparison with the *nanoloaded* antenna, the ohmic losses for different gap sizes are also shown (with dash lines). (b) Temperature distribution induced by a $\lambda = 10.6\,\mu$m incident radiation across the tapered Seebeck nanoantenna. *Top:* Map of the temperature (in a plane 50 nm below the dipole surface). *Bottom*: Temperature profile (along the antenna axis).

Once we have clarified that the receive dipoles resonate through its odd mode, we conduct efforts to evaluate the thermal gradients that light induce on the devices. For sake of clarity, we consider the particular case of a single monochromatic plane wave, with a 10.6 μm wavelength (~28.3 THz), as source of excitation. Therefore, we present a quite simple numerical manner to evaluate the thermal response of the dipoles and a manner to evaluate the Seebeck DC voltage.

The analysis consists in evaluating the temperature distribution induced by the incident radiation across the devices. From these results, the temperature difference between the center of the antenna and each open (ΔT_{Ni} and ΔT_{Ti}) can be extracted. Subsequently, the Seebeck voltage

Optics EXPRESS

V_{OC} developed at imaginary electrodes can be easily derived by using the relationship [43]:

$$V_{OC} = V_{OC(Ni)} + V_{OC(Ti)} = S_{Ni}\Delta T_{Ni} + S_{Ti}\Delta T_{Ti} \quad (2)$$

The voltage V_{OC} is interpreted as the series combination of the Seebeck voltage across the nickel arm $V_{OC(Ni)} = S_{Ni}\bullet\Delta T_{Ni}$, and across the titanium arm $V_{OC(Ti)} = S_{Ni}\bullet\Delta T_{Ni}$. It is worth noting that two different temperature increments should be considered since the end of each arm does not reach the same steady-temperature due the difference in their thermal conductivity.

The thermal simulations of the receiving dipole are performed in COMSOL Multi-Physics because it includes a platform where both the electromagnetic and thermal domains are fully integrated, as required for the analysis. The numerical model was built by considering the heating of the dipole as a full optical problem [44]. Under this consideration, we first perform the electromagnetic simulations to evaluate the heat density q [W/m^3] due to resistive losses induced by the single monochromatic PL plane wave (at 10.6 μm). The heat density is found by using the Joule effect expression $q = J\bullet E$, where E denotes the electric field distribution inside the dipole and J the resonant current. Then, we use the heat density to numerically solve the conduction heat-transfer equation and find the steady-state temperature distribution $T(r)$ of the thermal system, inside and outside the dipole (this, by imposing that the substrate is thermalized at room temperature).

The map of the temperature (in a plane 50 nm below the dipole surface) and the temperature profile (along the antenna axes) induced by the monochromatic plane wave at 10.6 μm, are shown in Fig. 3(b). Due to its lower thermal conductivity, the titanium arm shows a higher temperature increment ($\Delta T_{Ti} \sim 146$ mK) than the nickel arm ($\Delta T_{Ni} \sim 143$ mK). The Seebeck voltage associated to the thermal gradient can reach a value $V_{OC} \approx 3.8$ μV. Under impedance match conditions (both, electric and thermal), the antenna can deliver to an external acquisition system a total power ~ 53.1 fW. This value is obtained by using the expression $P = V_{OC}{}^2/4R_{int}$, where R_{int} refers to the DC resistance of the tapered dipole, here calculated to be ~ 68 Ω [45].

It is worth noting that the rise of temperature depends on the intensity of the incident light: the higher the intensity the higher the temperature increments. In this study, we have fixed the amplitude of the monochromatic plane wave to the arbitrary value of $|\boldsymbol{E}_0| \sim 29\times10^3$ [V/m], leading to a time-averaged magnitude of Pointing's Vector of 117 W/cm^2, value used in typical LWIR antennas measurements set-ups [46]. The effects of the irradiance on the efficiency of the devices are out of the scope of this contribution.

4. Particle swarm optimization of the bimetallic dipoles

Once we have properly determined and analyzed the resonances, and the Seebeck voltage that tapered dipoles can exhibit, we conduct efforts to find the geometrical parameters that optimize the thermal gradients of the antennas, and therefore their performance as harvesters.

To achieve this task, we use a particle swarm optimization (PSO) algorithm routine. The PSO program (implemented in Matlab), communicates with the numerical solver COMSOL Multi-Physics through the LiveLink MatLab link tool (provided by the COMSOL software package). The solver obtains both, the power dissipated along the antenna as ohmic losses P [W], and the thermal gradients ΔT_{Ni} and ΔT_{Ti} of the given geometry, whose relative relevance is measured through a proposed fitness function f (see Eq. (3)). The PSO optimizer subsequently evaluates the value of the fitness function and then updates the dimensions of the nanoantennas in order to minimize it at wavelengths around 10.6 μm (28.3 THz).

The fitness function here suggested is a quite simple linear combination of the thermal gradients (ΔT_{Ni} and ΔT_{Ti}) along the dipole, and the wavelength $\lambda_{max(Q)}$ at which the heat by ohmic losses is maximum. The expression is given by:

$$f = -c_1 \bullet (S_{Ni}\Delta T_{Ni} + S_{Ti}\Delta T_{Ti}) + c_2 \bullet |\lambda_{max(Q)} - 10.6\mu m| \quad (3)$$

Optics EXPRESS

where c_1 and c_2 are positive constants that equalize the contribution of the two terms of the expression. On the one hand, the algorithm will tune the maxima of the ohmic losses to the desired operation wavelength (10.6 μm) by vanishing the second term of the fitness function; this means the dipoles will resonate around this wavelength. On the other hand, the algorithm will increase as much as possible the Seebeck voltage by minimizing as much as possible the first term of the fitness function. The PSO algorithm is a powerful tool that simultaneously minimizes both terms.

The particle swarm algorithm is configured with 20 particles, 200 generations. The cognitive and social parameters determine the search speed and the convergence speed, which are selected as 0.2 respectively. The geometric parameter dimensions to optimize the cost function are subject to restrictions to ensure its construction and in turn maintain the aspect ratio of the nano-antenna. The parameters L_1, L_2, L_3, W_1, W_2, W_3 and L must be greater than 10 nm. W_1 must be greater than W_2 and this greater than W_3 ($W_1 > W_2 > W_3$). To keep the total antenna length limited, the parameter L_1 is calculated in function of L_2 and L_3 ($L_1 = L - L_2 - L_3 - 20$ nm). In order to accelerate the execution of the optimization, the COMSOL simulation of a one particle is run when all the restrictions established above are met; otherwise, the particle is considered with a poor performance.

The PSO algorithm was ran by taking as initial conditions the geometrical parameters of the dipole geometry shown in Fig. 1. The algorithm proposed a total amount of 4000 geometries and only explored seventeen hundred eighty-five different dipole geometries (fulfilling the constraint) during the minimization of the fitness function. The evolution of the fitness function, shown in Fig. 4(b), is arranged in a decreasing manner, with respect to the number of total dipoles that were tested. The geometry proposed by the PSO algorithm, which reduces the best the fitness function, is shown in Fig. 4(a). Its dimensions are $W_1 = 80$ nm, $W_2 = 120$ nm, $W_3 = 200$ nm, $L_1 = 50$ nm, $L_2 = 200$ nm, $L_3 = 700$ nm and $T = 200$ nm.

To unveil the improvement obtained via the proposed fitness function, the expected Seebeck voltage is plotted in Fig. 4(c). First at all, the voltage does not change continuously with the minimization of the fitness function f, instead, it arranges in well-defined lines with positive slope. By regarding the frequencies at which the explored dipoles resonate (indicated by the labels next the lines) we can remark that lines appear because the numerical simulations were based on a discrete frequency sweep (with steps of 0.5 THz). Particularly, each line contains the structures whose resonances are equally far from the target frequency (~28 THz). As sated above, the dipoles meet the desired resonance frequency only by vanishing the second term of the function f; however, the changes of this second term are discrete. Secondly, once the desired resonance frequency is reached, the algorithm reduces the fitness function by increasing the magnitude of the Seebeck voltage up to ~10.4 μV.

To highlight the importance of these results, we must state that conventional half-wave dipoles typically exhibit Seebeck voltages around ~3.2 μV under the same irradiance conditions [47]. Hence, by using the here optimized tapered dipole, the performance of the antennas as harvesters can be increased by 220%.

It is worth to mention that other optimization concepts have been explored elsewhere in order to increase the performance of the long-wavelength infrared-regime antennas (LWIR), such as the thermal isolation of devices from the substrate (air-bridge technology), which is intended to avoid the flux of heat towards the substrate [47]. For the case of conventional half-wave dipoles (in the LWIR regime) such a strategy increases the performance of the devices by a factor 400%. Even though the air-bridge technology substantially improves the efficiency of the nano-antennas, it adds more difficulties on their manufacture, so, other closely related concept for improvements were then considered.

Optics EXPRESS

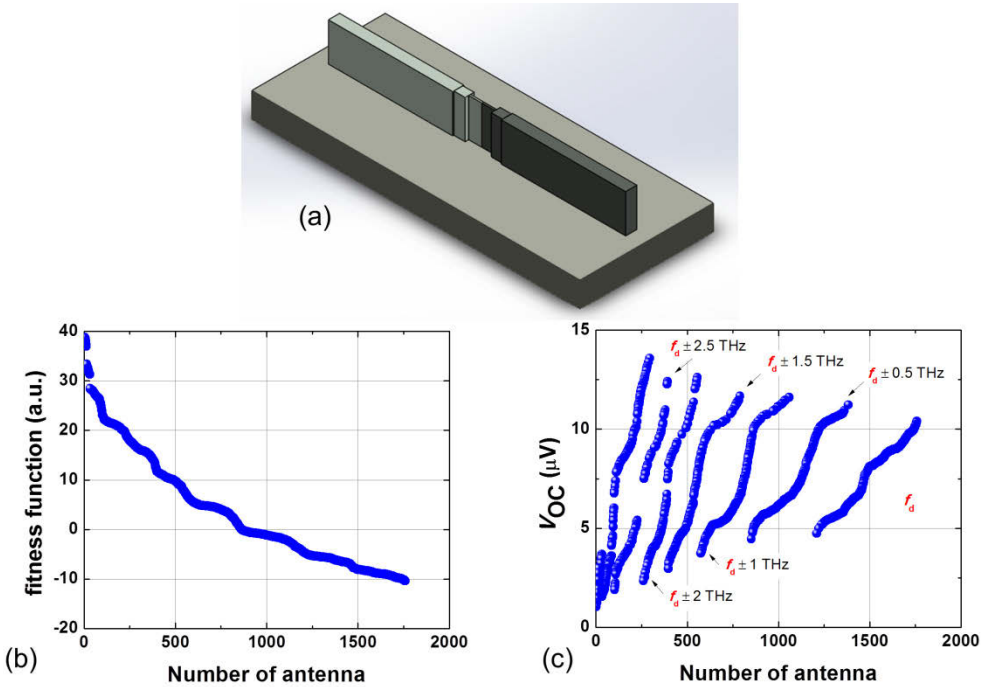

Fig. 4. PSO optimization of Seebeck nanoantennas. (a) Schema representing the dipole antenna geometry optimized through the fitness function. (b) Evolution of the fitness function respect to the number of antennas tested. (c) Seebeck voltage corresponding to each tested geometry.

5. Geometrical trends

As shown by the results, the PSO algorithm is an accurate tool to optimize the response of the Seebeck dipole. To unveil and understand the physical mechanism behind the response of the optimized dipole, we analyze the effects of each geometrical parameter on both, the Seebeck voltage and the fitness function. At the light of the geometrical trends, we will be able to identify and measure the contribution of the possible mechanisms. It is worth noting that one of the main advantages of the optimization algorithm used is the search for solutions in multidimensional spaces, so all parameters are changed at once. This can give us an idea of the real impact of each of the parameters on the cost function by analyzing the results because multiple parameters are explored at the same time.

Throughout Figs. 5(a)–5(f), we can follow the evaluation of the Seebeck voltage with respect to the size of each parameter tested during the optimization process. We use a color map plot, where blue (yellow) indicates low (high) values of the fitness function; those are associated to dipoles with optimal (poor) performance. For clarity, the results for the proposed initial dipole geometry, the optimized geometry, and the worst dipole proposed by the algorithm, are highlighted by square, asterisk and diamond markers in red, respectively. From these results, we can remark that well-defined paths indicating the evolution of the optimization appear on the figure. In this way, it is easy to see that both parameters, the fitness function and the Seebeck voltage, increase as the width of the tapered sections (W_1, W_2, W_3) is reduced.

By comparing the size of the three different widths required for the best dipoles, we remark that the two steps closer to the center of the antenna (or the bimetallic junction) are the most important parameters; the narrower the steps W_3 and W_2 the higher the Seebeck voltage. In

Optics EXPRESS

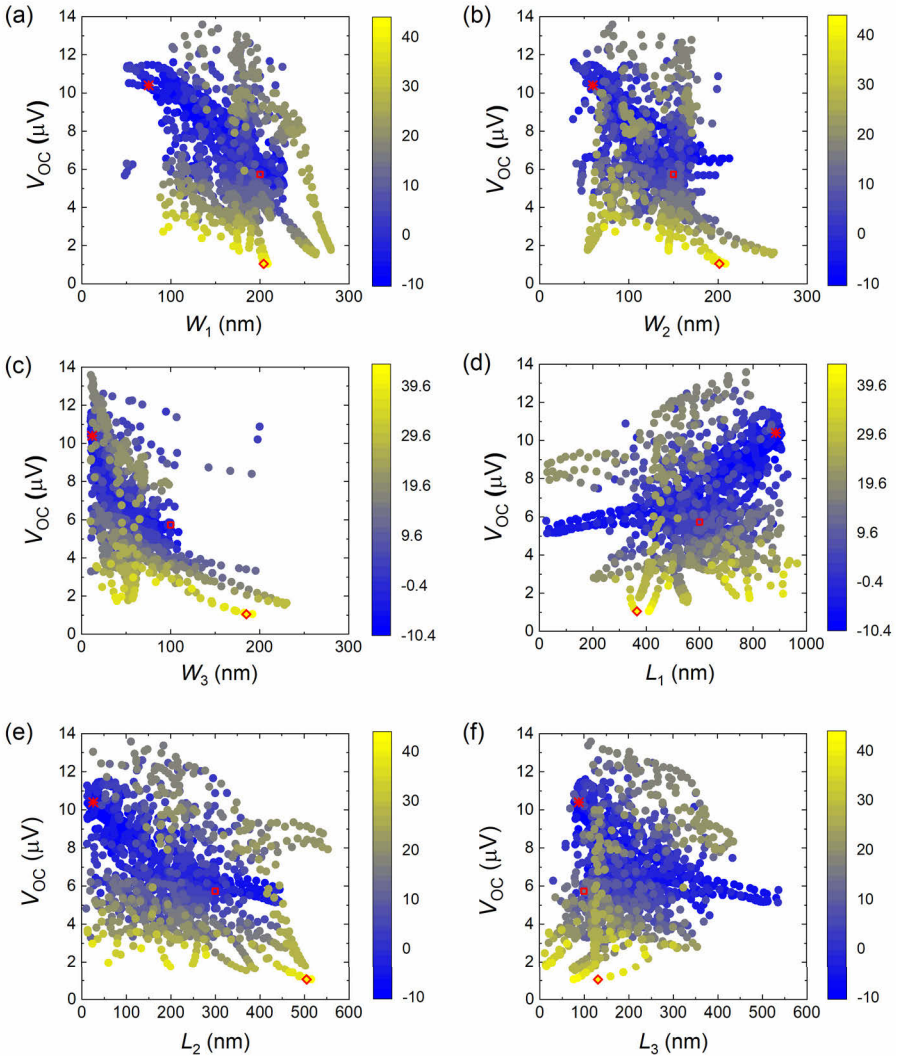

Fig. 5. Evolution of the Seebeck voltage with respect to the size of each parameter tested during the optimization process. W_1, W_2 and W_3 are the widths of the tapered sections; L_1, L_2 and L_3 are the lengths of the tapered sections. Red squares highlight the dimensions of the initial geometry; asterisks indicate the dimensions of the optimized geometry; diamonds stand for the dimensions of the worst dipole geometry. The color bar is associated to the value of the fitness function, which the PSO algorithm look to minimize.

Optics EXPRESS

particular, W_3 tends to zero while W_2 reaches a dozen of nanometers ($W_3 < W_2$). This means that tapered dipoles with a well-defined sharp tip at their center will exhibit a better performance as harvesters.

Furthermore, the results bring out a remarkable dependence of the Seebeck voltage on the length of the outermost tapered section L_1, the longest length being required. Complementary, the lengths of the internal sections L_2 and L_3 must be as short as possible; it must be noted that the step closer to the center is larger than the middle step ($L_3 > L_2$). As a consequence, the optimized tapered dipoles resemble sharp-tip conventional half-wave dipole loaded with a simple short filament [36]. All these results support the idea, somehow expected, that the performance of devices as harvesters depends on the local geometry around the bi-metallic interface (*i.e.* the center of the antenna).

6. Intrinsic impedance versus thermal impedance of bimetallic dipoles

Once we have unveiled the geometrical trends required by the optimal dipoles, we make an analysis of the physical reasons behind it. As stated above, the best antennas look like sharp-tip conventional half-wave dipoles loaded with a simple short filament. The local geometry around the bimetallic interface defined by those geometries, mainly affects the intrinsic impedance of the dipole Z_{dip}, and its thermal impedance Z_{th}. We therefore evaluate the contribution of these two mechanisms to the response of the device.

It has been well-stablished that the intrinsic impedance of a tapered dipole (at optical frequencies) depends on its geometry [24]. In contrast to the impedance value of conventional half-wave dipoles (~60 Ω), the impedance of a tapered antenna can be tuned from few dozens to few hundreds of ohms by adjusting its geometry [24]. According to the antenna theory [48], the impedance of the antenna affects the power that can be transmitted to its center (and so the heating of the bimetallic interface). The optical power P (in watts) that receiving antennas collect and transmit to their center (or load) can be evaluated by means of the relationship:

$$P = Z_{dip} \bullet |I_{SC}|^2 \tag{4}$$

where Z_{dip} and I_{SC} correspond to the intrinsic impedance and the short-circuit resonance current at the center of the antenna, respectively [48]. The impedance of a tapered dipole can change by several orders of magnitude, hence a strong dependence on this parameter could be expected. To clarify this point, we evaluate, by using the method described in section two, the real R_{dip} and imaginary X_{dip} parts of the intrinsic impedance of the dipoles explored by the PSO algorithm. The obtained plot is shown in Fig. 6(a). The impedance is plotted for the desired operation frequency ~28 THz. The results clearly show that the impedance of the optimized dipoles is consistently ~ 60 Ω. This means that heat due to ohmic losses is similar for all the geometries. The impedance dispersion exhibited by the first explored geometries (the non-optimized ones), is expected since they do not resonate at the desired frequency, so, their reactance does not vanish. All these results indicate that the mechanism beneath the optimized tapered dipoles does not rely on the optical and electrical behavior.

At the light of these results, we then analyze how the thermal behavior depends on the dipole geometry. Because the paths of heat conduction are different for each explored geometry, their thermal gradients will be too. To get insight on this concern, we evaluate the thermal impedance of the geometries. This parameter accurately reflects the heat-dissipating capability of thermal engines and accounts for all the interfacial effects and heat conduction paths.

The impedance of a thermal engine Z_{th} is defined as the temperature rise ΔT per watt of dissipated power P, passing through the interface. It is simply calculated by the relationship [49]:

$$Z_{th} = \frac{\Delta T}{P} \tag{5}$$

Optics EXPRESS

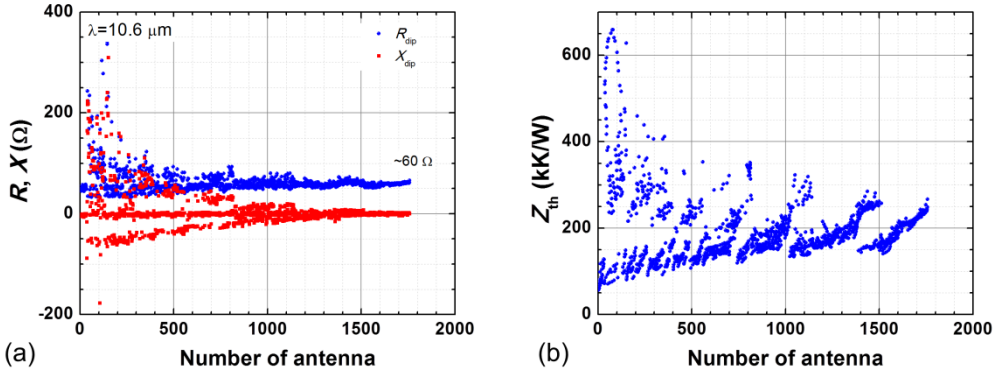

Fig. 6. (a) Evolution of the intrinsic impedance respect to the number of antennas tested, with R (*red dots*) being the real and X (*blue squares*) the imaginary parts of the impedance. (b) Impedance of the equivalent thermal engines.

indicating that the higher the thermal impedance, the lower the heat flux through the interface, and so, the higher its temperature.

For the case of the tapered dipoles, which are composed by arms of dissimilar metals, the total impedance Z_{th} can be interpreted as the parallel combination of the nickel arm impedance $Z_{th(Ni)}$ and the titanium arm impedance $Z_{th(Ti)}$. Therefore, the impedance Z_{th} of the Seebeck dipoles can be obtained (if the thermal impedance of each arm is known) through the relationship:

$$Z_{th} = \frac{Z_{th(Ni)} \bullet Z_{th(Ti)}}{Z_{th(Ni)} + Z_{th(Ti)}} \tag{6}$$

At this concern, the thermal impedance of the arms can be obtained by driving the bimetallic interface of the tapered dipole with a surface heat-source P (by means of numerical simulations), and by obtaining the temperature increment induced in each arm ΔT_{Ni} and ΔT_{Ti}. By this means, $Z_{th(Ni)}$ and $Z_{th(Ti)}$ are obtained by simply using the relationship (5), and Z_{th} from the relationship (6).

The thermal impedance obtained via simulations, for the total amount of explored dipoles, is shown in Fig. 6(b). In contrast to the intrinsic impedance, the thermal impedance exhibits a strong dependence on the geometry, ranging from a few dozen to a few hundred of kilo kelvins per watts. Regarding this, we can remark that the thermal impedance arranges in vertical lines with positive tendency, analogous to the Seebeck voltage curve in Fig. 4(c). Results show in a clear manner that the geometries with the highest impedance are those that exhibit the highest rise of temperature, and thus the highest Seebeck voltage. We can note that this is true even if the dipoles do not resonate at frequencies around 28.3 THz (10.6 μm).

All these results unveil that the main mechanism beyond the performance of the optimized dipoles is their thermal impedance and not the intrinsic impedance of the dipoles (or the optical properties).

7. Conclusions

A three tapered Seebeck nano-antenna architecture was investigated as an efficient design to gather energy in the infra-red band. First, the multi-resonant behavior of this design was evaluated by implementing the so-called *nanoloading* technique. The ohmic losses, related to the conversion of electromagnetic energy into induced AC currents, where then used as a figure-of-merit; its frequency dependence being thus determined. Subsequently, from the heat density associated to the resistive losses, the temperature gradients across the devices were evaluated; and thus the

Optics EXPRESS

Seebeck voltage of the antenna was calculated. The particle swarm optimization PSO algorithm was then implemented in order to obtain the antenna dimensions that optimize the thermal gradients, and hence the retrieved Seebeck voltages. Further, the geometrical trends, meaning the influence of each geometrical variable on the resulting voltage, were analyzed. The results strongly indicating that the most inner steps of the tapered dipole lead the performance of the devices as optimal harvesters. Moreover, by evaluating the evolution of the thermal impedance for all of the antenna geometries it was found that this parameter is the one determining the ultimate thermoelectric response, overriding the intrinsic (electric) impedance.

Funding

Sistema Nacional de Investigadores (48506, 56874); Consejo Nacional de Ciencia y Tecnología (FORDECYT-297497).

Disclosures

The authors declare that there are no conflicts of interest related to this article.

References

1. N. M. Haegel, H. Atwater Jr, T. Barnes, C. Breyer, A. Burrell, Y.-M. Chiang, S. De Wolf, B. Dimmler, D. Feldman, S. Glunz, J. C. Goldschmidt, D. Hochschild, R. Inzunza, I. Kaizuka, B. Kroposki, S. Kurtz, S. Leu, R. Margolis, K. Matsubara, A. Metz, W. K. Metzger, M. Morjaria, S. Niki, S. Nowak, I. M. Peters, S. Philipps, T. Reindl, A. Richter, D. Rose, K. Sakurai, R. Schlatmann, M. Shikano, W. Sinke, R. Sinton, B. J. Stanbery, M. Topic, W. Tumas, Y. Ueda, J. van de Lagemaat, P. Verlinden, M. Vetter, E. Warren, M. Werner, M. Yamaguchi, and A. W. Bett, "Terawatt-scale photovoltaics: Transform global energy," Science **364**(6443), 836–838 (2019).
2. P. K. Nayak, S. Mahesh, H. J. Snaith, and D. Cahen, "Photovoltaic solar cell technologies: analysing the state of the art," Nat. Rev. Mater. **4**(4), 269–285 (2019).
3. A. Polman, M. Knight, E. C. Garnett, B. Ehrler, and W. C. Sinke, "Photovoltaic materials: Present efficiencies and future challenges," Science **352**(6283), aad4424 (2016).
4. K. Tanabe, "A review of ultrahigh efficiency III-V semiconductor compound solar cells: Multijunction Tandem, Lower Dimensional, Photonic Up/Down Conversion and Plasmonic Nanometallic Structures," Energies **2**(3), 504–530 (2009).
5. M. Yamaguchi, T. Takamoto, K. Araki, and N. Ekins-Daukes, "Multi-junction III–V solar cells: current status and future potential," Sol. Energy **79**(1), 78–85 (2005).
6. T. Saga, "Advances in crystalline silicon solar cell technology for industrial mass production," NPG Asia Mater. **2**(3), 96–102 (2010).
7. N. Fatemi, J. Lyons, and M. Eskenazi, "Qualification and production of Emcore ZTJ solar panels for space missions," in *Proceedings of IEEE 39th Photovoltaic Specialists Conference* (IEEE, 2013), pp. 2793–2796.
8. Y. Bi, A. Bertran, S. Gupta, I. Ramiro, S. Pradhan, S. Christodoulou, S.-N. Majji, M. Z. Akgula, and G. Konstantatos, "Solution processed infrared- and thermophotovoltaics based on 0.7 eV bandgap PbS colloidal quantum dots," Nanoscale **11**(3), 838–843 (2019).
9. A. Luque, A. Martí, and C. Stanley, "Understanding intermediate-band solar cells," Nat. Photonics **6**(3), 146–152 (2012).
10. A. Luque, E. Antolín, P. G. Linares, I. Ramiro, A. Mellor, I. Tobías, and A. Martí, "Interband optical absorption in quantum well solarcells," Sol. Energy Mater. Sol. Cells **112**, 20–26 (2013).
11. M. Y. Levy and C. Honsberg, "Solar cell with an intermediate band of finite width," Phys. Rev. B **78**(16), 165122 (2008).
12. Y. Okada, N. J. Ekins-Daukes, T. Kita, R. Tamaki, M. Yoshida, A. Pusch, O. Hess, C. C. Phillips, D. J. Farrell, K. Yoshida, N. Ahsan, Y. Shoji, T. Sogabe, and J.-F. Guillemoles, "Intermediate band solar cells: Recent progress and future directions," Appl. Phys. Rev. **2**(2), 021302 (2015).
13. A. Luque and A. Martí, "Towards the intermediate band," Nat. Photonics **5**(3), 137–138 (2011).
14. A. Balčytis, M. Ryu, S. Juodkazis, and J. Morikawa, "Micro-thermocouple on nano-membrane: thermometer for nanoscale measurements," Sci. Rep. **8**(1), 6324 (2018).
15. G. P. Szakmany, A. O. Orlov, G. H. Bernstein, and W. Porod, "Cavity-Backed Antenna-Coupled Nanothermocouples," Sci. Rep. **9**(1), 9606 (2019).
16. G. P. Szakmany, A. O. Orlov, G. H. Bernstein, and W. Porod, "Polarization-Dependent Response of Single- and Bi-Metal Antenna-Coupled Thermopiles for Infrared Detection," IEEE Trans. Terahertz Sci. Technol. **5**(6), 884–891 (2015).
17. B. Szentpáli, P. Basa, P. Fürjes, G. Battistig, I. Bársony, G. Károlyi, T. Berceli, V. Rymanov, and A. Stöhr, "Thermopile antennas for detection of millimeter waves," Appl. Phys. Lett. **96**(13), 133507 (2010).

Optics EXPRESS

18. E. Briones, J. Briones, A. Cuadrado, J. C. Martinez-Anton, S. McMurtry, M. Hehn, F. Montaigne, J. Alda, and F. J. Gonzalez, "Seebeck nanoantennas for solar energy harvesting," Appl. Phys. Lett. **105**(9), 093108 (2014).
19. M.-M. Mennemanteuil, G. Colas-des-Francs, M. Buret, A. Dasgupta, A. Cuadrado, J. Alda, and A. Bouhelier, "Laser-induced thermoelectric effects in electrically biased nanoscale constrictions," Nanophotonics **7**(12), 1917–1927 (2018).
20. F. Lu, J. Lee, A. Jiang, S. Jung, and M. A. Belkin, "Thermopile detector of light ellipticity," Nat. Commun. **7**(1), 12994 (2016).
21. B. Mora-Ventura, R. Díaz de León, G. García-Torales, J. L. Flores Nuñez, J. Alda, and F. J. González, "Responsivity and resonant properties of dipole, bowtie, and spiral Seebeck nanoantennas," J. Photonics Energy **6**(2), 024501 (2016).
22. P. R. Wiecha, A. Arbouet, C. Girard, A. Lecestre, G. Larrieu, and V. Paillard, "Evolutionary multi-objective optimization of colour pixels based on dielectric nanoantennas," Nat. Nanotechnol. **12**(2), 163–169 (2017).
23. M. N. Ab Wahab, S. Nefti-Meziani, and A. Atyabi, "Comprehensive Review of Swarm Optimization Algorithms," PLoS One **10**(5), e0122827 (2015).
24. Y. M. El-Toukhy, M. Hussein, M. F. O. Hameed, A. M. Heikal, M. M. Abd-Elrazzak, and S. S. A. Obayya, "Optimized tapered dipole nanoantenna as efficient energy harvester," Opt. Express **24**(14), A1107–A1122 (2016).
25. Y. M. El-Toukhy, M. Hussein, M. F. O. Hameed, and S. S. A. Obayya, "Characterization of Asymmetric Tapered Dipole Nanoantenna for Energy Harvesting Applications," Plasmonics **13**(2), 503–510 (2018).
26. A. Graf, M. Arndt, M. Sauer, and G. Gerlach, "Review of micromachined thermopiles for infrared detection," Meas. Sci. Technol. **18**(7), R59–R75 (2007).
27. M. Ito, D. Setoyama, J. Matsunaga, H. Muta, K. Kurosaki, M. Uno, and S. Yamanaka, "Electrical and thermal properties of titanium hydrides," J. Alloys Compd. **420**(1-2), 25–28 (2006).
28. W. Zhu, G. Zheng, S. Cao, and H. He, "Thermal conductivity of amorphous SiO2 thin film: A molecular dynamics study," Sci. Rep. **8**(1), 10537 (2018).
29. S. W. Fong, A. Sood, L. Chen, N. Kumari, M. Asheghi, K. E. Goodson, G. A. Gibson, and H. S. P. Wong, "Thermal conductivity measurement of amorphous dielectric multilayers for phase-change memory power reduction," J. Appl. Phys. **120**(1), 015103 (2016).
30. A. Böhme, F. Sterl, E. Kath, M. Ubl, V. Manninen, and H. Giessen, "Electrochemistry on Inverse Copper Nanoantennas: Active Plasmonic devices with Extraordinarily Large Resonance Shift," ACS Photonics **6**(8), 1863–1868 (2019).
31. Z. Pirzadeh, T. Pakizeh, V. Miljkovic, C. Langhammer, and A. Dmitriev, "Plasmon–Interband Coupling in Nickel Nanoantennas," ACS Photonics **1**(3), 158–162 (2014).
32. M. W. Knight, L. Liu, Y. Wang, L. Brown, S. Mukherjee, N. S. King, H. O. Everitt, P. Nordlander, and N. J. Halas, "Aluminum Plasmonic Nanoantennas," Nano Lett. **12**(11), 6000–6004 (2012).
33. A. Alù and N. Engheta, "Input Impedance, Nanocircuit Loading, and Radiation Tuning of Optical Nanoantennas," Phys. Rev. Lett. **101**(4), 043901 (2008).
34. A. Alù and N. Engheta, "Tuning the scattering response of optical nanoantennas with nanocircuit loads," Nat. Photonics **2**(5), 307–310 (2008).
35. Y. Xu, E. Tucker, G. Boreman, M. B. Raschke, and B. A. Lail, "Optical Nanoantenna Input Impedance," ACS Photonics **3**(5), 881–885 (2016).
36. S. Dong, K. Zhang, Z. Yu, and J. A. Fan, "Electrochemically Programmable Plasmonic Antennas," ACS Nano **10**(7), 6716–6724 (2016).
37. E. D. Palik, *Handbook of Optical Constants of Solids* Vol. 3 (Academic, 1997).
38. K. A. Obeidat, B. D. Raines, and R. G. Rojas, "Discussion of series and parallel resonance phenomena in the input impedance of antennas," Radio Sci. **45**(6), RS6012 (2010).
39. W. Zhu, M. G. Banaee, D. Wang, Y. Chu, and K. B. Crozier, "Lithographically Fabricated Optical Antennas with Gaps Well Below 10 nm," Small **7**(13), 1761–1766 (2011).
40. D. P. Fromm, A. Sundaramurthy, P. J. Schuck, G. Kino, and W. E. Moerner, "Gap-Dependent Optical Coupling of Single "Bowtie" Nanoantennas Resonant in the Visible," Nano Lett. **4**(5), 957–961 (2004).
41. C. Menzel, E. Hebestreit, S. Mühlig, C. Rockstuhl, S. Burger, F. Lederer, and T. Pertsch, "The spectral shift between near- andfar-field resonances of opticalnano-antennas," Opt. Express **22**(8), 9971–9982 (2014).
42. J. Zuloaga and P. Nordlander, "On the Energy Shift between Near-Field and Far-Field Peak Intensities in Localized Plasmon Systems," Nano Lett. **11**(3), 1280–1283 (2011).
43. D. M. Rowe, *Thermoelectrics Handbook: Macro to Nano* (CRC, 2006).
44. W. Zhao and J. M. Karp, "Nanoantennas heat up," Nat. Mater. **8**(6), 453–454 (2009).
45. J. P. Carmo, L. M. Goncalves, and J. H. Correia, "Micro and nanodevices for thermoelectric converters," in *Scanning Probe Microscopy in Nanoscience and Nanotechnology 2*, B. Bhushan, ed. (Springer, 2011).
46. F. J. González and G. D. Boreman, "Comparison of dipole, bowtie, spiral and log-periodic IR antennas," Infrared Phys. Technol. **46**(5), 418–428 (2005).
47. E. Briones, C. Kuri, I. Cortes-Mestizo, J. Briones, and H. Vilchis, "Numerical conversion efficiency of thermally isolated Seebeck nanoantennas," AIP Adv. **6**(11), 115018 (2016).
48. C. A. Balanis, *Antenna Theory: Analysis and Design* (John Wiley & Sons, 1996).
49. F. J. González, "Thermal-impedance simulations of antenna-coupled microbolometers," Infrared Phys. Technol. **48**(3), 223–226 (2006).